

# **Medium Energy Proton and Electron Detector**

## **Precipitating Electron data set (MPE)**

### I. Introduction

Accurately measuring and quantifying trapped and precipitating electrons is an important aspect of magnetosphere science as well as atmospheric science. The data set presented here attempts to offer a solution to this problem using the Medium Energy Proton and Electron Detector (MEPED) detectors aboard the NOAA's Polar-orbiting Observational Environmental Satellites (POES) and the European Space Agency MetOp satellites (METOP). The reason for choosing these instruments is the POES satellites have the longest running and highest spatial coverage of any other instrument measuring trapped and precipitating electrons. The original SEM-1 MEPED instruments date back to 1978 flying on the TIROS-N satellites. The introduction of the SEM-2 instruments was presented on the NOAA-15 launch in July of 1998. The data set introduced here is built exclusively from the SEM-2 instruments, however data sets that utilize the SEM-1 detectors do exist (*Asikainen, 2019*).

The SEM/2 MEPED instruments, which are described in more detail by *Evans and Greer (2006)* and *Green, (2013)*, are onboard the NOAA POES numbers 15 through 19 as well as all three European Space Agency (ESA) MetOp satellites. This gives the MPE data set a date range from late 1998 through the present day; date ranges for each satellite can be found in Table 1. The MEPED instruments have two

<b><u>Satellite</u></b>	<b><u>Data Window</u></b>
<b>NOAA-15</b>	1998-07-01 – present
<b>NOAA-16</b>	2001-01-10 – 2014-06-06
<b>NOAA-17</b>	2002-07-12 – 2013-04-10
<b>NOAA-18</b>	2005-06-07 – present
<b>NOAA-19</b>	2009-02-23 – present
<b>MetOp-01</b>	2012-10-03 – present
<b>MetOp-02</b>	2006-12-03 – present
<b>MetOp-03</b>	2019-01-01 – present

**Table 1:** All satellites that have SEM/2 MEPED instruments, and their dates of operation. Some data gaps exist within the data window.

telescopes for proton detection and two telescopes for electron detection that are used in this data set. Each pair of telescopes includes one that points toward the zenith with a 9° offset (“0-degree detector”) and one that points in the anti-ram direction with a 9° offset (“90-degree detector”); both telescopes have a 30° field of view. As depicted in Figure 1, the proton telescopes have five broadband channels within the energy range

from 30 keV – 6900 keV, and a P6 channel that detects protons with energies > 6900 keV. The P6 channel is also sensitive to relativistic electrons and can be used as a proxy for electrons with energies greater than ~700 keV in the absence of protons (*Yando et al., 2011*). The electron telescopes contain three, overlapping broadband channels coined E1 – E3 that nominally detect electrons with energies of 30 – 2500 keV, 100-2500 keV, and 300-2500 keV, respectively. The data set described here includes the P6 channel as a virtual E4 channel that measures electrons with energies > ~700 keV in the absence of protons. The raw data from MEPED are proton and electron count rates that are sampled every other second; these raw data are then averaged every 16-seconds. It is important to note that the three physical electron channels are affected by proton contamination (*Evans and Greer, 2006*). Figure 1 demonstrates the proton energies for which each of the electron channels are impacted. For example, the E1 channel can be affected by protons ranging in energy from 200 keV through 3 MeV. Thus, before using the electron data, a proton contamination removal algorithm must be applied.

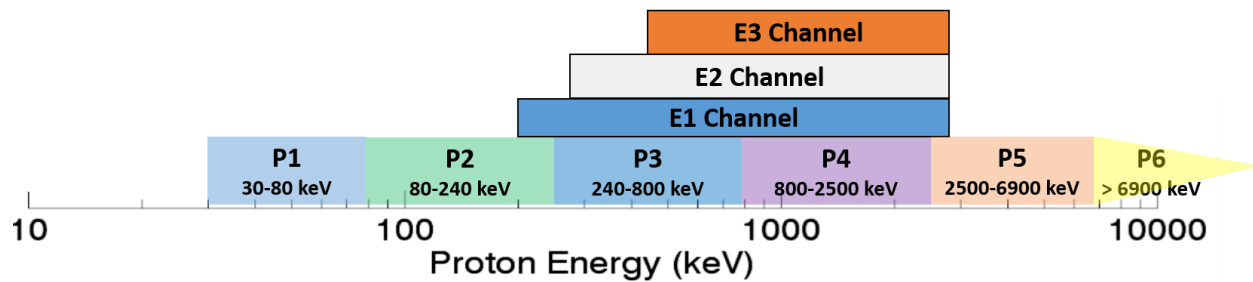


**Figure 1:** Schematic to show proton contamination in the MEPED electron channels. Colored boxes on the bottom row indicate the MEPED proton channels P1-P6, with their energy ranges. Colored boxes above indicate the three electron channels (labeled E1, E2, E3) that suffer from proton contamination. The horizontal axis refers only to proton energy, not to energies of the electron channels (see the text).

The Medium Energy Proton and Electron Detector Precipitating Electron data set (MPE) has three levels of products that will be explained in detail below. The Level 1 product converts the integral broadband electron channels into differential electron flux with 27 energy levels ranging from 27 keV through 8.9 MeV. The product includes data from both the 0° and 90° detectors and is available at the measuring locations and times of the MEPED satellites. The Level-2 product will take the differential electron flux and calculate an estimate of the bounce-loss cone (BLC) flux precipitating at the satellite location. Once again, this product will be available at the times and locations of the satellites. The Level-3 product will create 2D maps of the BLC flux on 27 energy levels for use in modeling studies or comparisons with other instrumentation. The following section will explain the creation of the three data products in detail.

## II. Data Product Description

### A. Level 1 Data Product

The first step in creating the MPE data set is taking the four electron channels (E1-E3 + P6) and calculating a best fit differential flux spectrum for each measurement point. Before this can be done however, proton contamination must be removed from the electron channels. As shown in Figure 1, the proton channels which affect the electron channels are not a one-to-one correlation. For example, the E1 channel receives proton contamination from four of the proton channels. Therefore, one possible method of estimating the proton contamination for each electron channel is to convert the proton channels into a differential flux spectrum and integrate between the energies which contaminate each electron channel. While it is true that the proton channels contain electron contamination as well ([reference](#)), it is thought to be small and will be ignored in the following methodologies. The following steps will be taken to create the Level 1 data product, which is the differential electron flux at each measurement time and location:

- 1) Calculate the differential proton flux from the P1-P5 discrete channels.
- 2) Integrate the proton flux between the energies by which the three electron channels are affected:
- 3) Subtract the proton count rates determined by step 2 from the three original electron channels and add the P6 channel as a virtual E4 channel.
- 4) Calculate the differential electron flux using the E1-E4 channels along with estimated errors for the differential electron flux spectrum.

As mentioned, there are 27 evenly space energy bins on a logarithmic scale for the electron differential flux. Figure 2 depicts these energy bins along with the true range of the original electron channels.

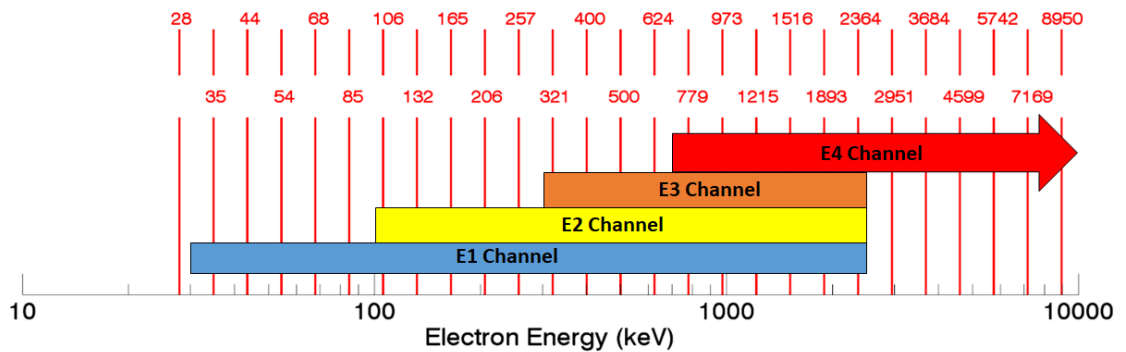


**Figure 2:** Energy ranges of the four integral electron channels (colored boxes). The red vertical lines indicate the midpoints of the logarithmic energy bins used to calculate differential electron flux spectra for the MPE data set.

The follow section is taken from *Peck et al.*, (2015) Appendix A to explain the mathematical details of how the proton and electron differential flux and errors are calculated.

---

## Appendix A

### POES MEPED Inversion Method

What follows here is the mathematical inversion method described in *O'Brien* [2011] and modified for use with the POES MEPED data. The goal of the method is to solve Equation 3.1:

$$\vec{y} \approx \vec{\lambda} = \delta t \int_0^\infty \vec{G}(E) \vec{f}(E) dE \quad (3.1)$$

Equation 1 can be discretized towards a numerical solution using the following equations:

$$\vec{y} \approx \vec{\lambda} = \underline{H} \vec{f} \quad (A1)$$

$$H_{ij} \approx \delta t G_i(E_j) \Delta E_j \quad (A2)$$

$$f_j = f(E_j) \quad (A3)$$

where  $\underline{H}$  is the inversion weighting function with dimensions  $N_y \times N_E$  and units of  $\text{cm}^2 \text{ sr sec keV}$ ,  $N_E$  is the number of energy bins, and  $f_j$  is the discretized form of  $f(E)$  from Equation 1 with units of  $\text{counts/cm}^2/\text{sr/sec/keV}$ . Equation A1 is a classic underdetermined, unconstrained, inversion equation. There are  $N_E$  unknown variables in  $\vec{f}$  and  $N_y$  equations, where  $N_y$  is less than  $N_E$ . The inversion technique that follows adds constraints to Equation A3 by taking a weighted average of possible spectral distributions to minimize the difference between  $\vec{y}$  and  $\vec{\lambda}$  in Equation A1.

The energy bins used in this inversion method are linearly separated in log space. The calculation of  $\Delta E_j$  in Equation A2 comes from a trapezoidal integral as follows:

$$\Delta E_j = \begin{cases} (E_{j+1} - E_j)/2 & j = 1 \\ (E_j - E_{j-1})/2 & j = N_E \\ (E_{j+1} - E_{j-1})/2 & \text{otherwise} \end{cases} \quad (A4)$$

A “penalty” function is defined to measure the likelihood of seeing the observed counts,  $\vec{y}$ ,

given the calculated expected counts,  $\vec{\lambda}$ . In other words, the penalty function is a calculation of how far apart  $\vec{y}$  and  $\vec{\lambda}$  are from each other including possible measurement errors. Observations and expected counts can differ due to various possible measurement error processes. We use Poisson and calibration errors as the only two possible measurement error processes in this correction method. The probability distribution for Poisson errors and calibration errors (given by a Gaussian distribution), are defined as:

$$p^{(P)}(y|\lambda) = \frac{\lambda^y e^{-\lambda}}{y!} \quad (\text{A5})$$

$$p^{(C)}(y|\lambda) = \frac{\exp[-((\ln y - \ln \lambda)/\delta y)^2/2]}{\sqrt{2\pi} y \delta y} \quad (\text{A6})$$

where  $p^{(P)}$  is the Poisson probability distribution of  $y$  given  $\lambda$  and  $p^{(C)}$  is the Calibration probability distribution of  $y$  given  $\lambda$ .

The penalty function is defined as the negative natural log of the probability distribution. Terms that are not dependent on  $\lambda$  are grouped together as a general constant. The penalty functions for Equations A5 and A6 are defined as:

$$\ell^{(P)}(\lambda) = -\ln p^{(P)} = \lambda - y \ln(\lambda) + \text{constants} \quad (\text{A7})$$

$$\ell^{(C)}(\lambda) = -\ln p^{(C)} = ((\ln y - \ln \lambda)/\delta y)^2/2 + \text{constants} \quad (\text{A8})$$

where  $\ell^{(P)}$  is the Poisson probability distribution penalty function,  $\ell^{(C)}$  is the calibration probability distribution penalty function, and  $\delta y$  is the Gaussian relative error, calculated to be 0.4 from bowtie analysis [Selesnick and Blake, 2000] for POES MEPED.

The derivatives and second derivatives of equations 8 and 9 with respect to  $\lambda$  will be needed later and are as follows:

$$\frac{d\ell^{(P)}}{d\lambda} = 1 - y/\lambda \quad (\text{A9})$$

$$\frac{d^2\ell^{(P)}}{d\lambda^2} = y/\lambda^2 \quad (\text{A10})$$

$$\frac{d\ell^{(C)}}{d\lambda} = (\ln \lambda - \ln y)/(\delta y)^2/\lambda \quad (\text{A11})$$

$$\frac{d^2\ell^{(P)}}{d\lambda^2} = (1 + \ln y - \ln \lambda)/(\lambda\delta y)^2 \quad (\text{A12})$$

Only one penalty function is used in this work for a given value of  $y$ . Therefore we select the larger source of error from either the Poisson counting error,  $1/\sqrt{y}$ , or the calibration Gaussian relative error,  $\delta y$ :

$$\ell_i = \begin{cases} \ell^{(P)} & y < (\delta y)^{-2} \\ \ell^{(C)} & \text{otherwise} \end{cases} \quad (\text{A13})$$

The summation of the selected penalty function from Equation A13 is a measure of how likely a spectral distribution,  $\vec{f}$ , is appropriately describing the original channel measurements,  $\vec{y}$ . Therefore, the goal of this inversion method is to minimize the following equation:

$$\ell(\vec{\lambda}) = \sum_i \ell_i(\lambda_i) \quad (\text{A14})$$

Converting the MEPED measurements into spectral flux is inherently an unconstrained problem. As such this inversion method assumes a set of possible spectra, and then weights them based on their ability to minimize Equation A14. Each spectral distribution are defined by a free parameters,  $q$ , and the total number of free parameters in each distribution is defined as  $N_q$ , where  $N_q$  is less than  $N_E$ . This effectively reduces the number of unknowns in the inversion of Equation A1. We use four spectral distributions to constrain our solution: power law (PL), exponential (EE), single relativistic Maxwellian (RM), and double relativistic Maxwellian (DM).

The PL spectrum,  $f^{(PL)}$ , requires two free parameters to fit (e.g.,  $N_q = 2$ ). We will need each spectral distribution along with its derivatives and second derivatives with respect to each free parameter. These equations are described as follows:

$$f^{(PL)}(E) = \exp(q_1 - q_2 \ln E) \quad (\text{A15})$$

$$\frac{\partial f^{(\text{PL})}}{\partial q_1} = f^{(\text{PL})} \quad (\text{A16})$$

$$\frac{\partial f^{(\text{PL})}}{\partial q_2} = -\ln(E)f(E) \quad (\text{A17})$$

$$\frac{\partial^2 f^{(\text{PL})}}{\partial q_1^2} = f^{(\text{PL})} \quad (\text{A18})$$

$$\frac{\partial^2 f^{(\text{PL})}}{\partial q_1 \partial q_2} = -\ln E f^{(\text{PL})} = \frac{\partial^2 f^{(\text{PL})}}{\partial q_2 \partial q_1} \quad (\text{A19})$$

$$\frac{\partial^2 f^{(\text{PL})}}{\partial q_2^2} = (\ln E)^2 f^{(\text{PL})} \quad (\text{A20})$$

EE spectrum is described by the following equations with two free parameters:

$$f^{(\text{EE})}(E) = \exp(q_1 + q_2 E) \quad (\text{A21})$$

$$\frac{\partial f^{(\text{EE})}}{\partial q_1} = f^{(\text{EE})} \quad (\text{A22})$$

$$\frac{\partial f^{(\text{EE})}}{\partial q_2} = E f^{(\text{EE})} \quad (\text{A23})$$

$$\frac{\partial^2 f^{(\text{EE})}}{\partial q_1^2} = f^{(\text{EE})} \quad (\text{A24})$$

$$\frac{\partial^2 f^{(\text{EE})}}{\partial q_1 \partial q_2} = E f^{(\text{EE})} = \frac{\partial^2 f^{(\text{EE})}}{\partial q_2 \partial q_1} \quad (\text{A25})$$

$$\frac{\partial^2 f^{(\text{EE})}}{\partial q_2^2} = E^2 f^{(\text{EE})} \quad (\text{A26})$$

RM spectrum has two free parameters and is described by the following equation, while it has derivatives as described by equations A22-A26 if  $f^{(\text{EE})}$  is replaced by  $f^{(\text{RM})}$ :

$$f^{(\text{RM})}(E) = E(1 + E/E_0/2)\exp(q_1 + q_2 E) \quad (\text{A27})$$

The DM spectrum has four free parameters as described below and has the same derivatives as the RM spectrum along with a straightforward extension of equations A22-A26 for the two additional free parameters:

$$f^{(\text{DM})}(E) = E(1 + E/E_0/2)[\exp(q_1 + q_2 E) + \exp(q_3 + q_4 E)] \quad (\text{A28})$$



In the RM and DM spectra, the constant  $E_0$  is used to represent the particle rest energy, which is equal to 511 keV in electrons and 938 MeV in protons.

The final step is to calculate the fit errors and combine the individual spectra to create a best multiple spectral fit. For a given spectrum,  $f^{(k)}(E)$ , the best fit is the minimization of  $\ell^{(k)}(\vec{\lambda})$  with respect to  $\vec{q}^{(k)}$ , yielding best fit free parameters,  $\hat{q}^{(k)}$ . For this case,  $k$  can be PL, EE, RM, or DM. The minimization routines require derivatives of  $\ell^{(k)}$  with respect to  $\vec{q}^{(k)}$ , given by:

$$\frac{\partial \ell}{\partial q_m} = \sum_i \frac{\partial \ell_i}{\partial \lambda_i} \sum_j \frac{\partial \lambda_i}{\partial f_j} \frac{\partial f_j}{\partial q_m} = \sum_i \frac{\partial \ell_i}{\partial \lambda_i} \sum_j H_{ij} \frac{\partial f_j}{\partial q_m} \quad (\text{A29})$$

To compute the error bars for a given spectral fit, the second derivative of the penalty function with respect to each free parameter is necessary. This can be represented by a Hessian using each combination of free parameters in the following form:

$$\frac{\partial^2 \ell}{\partial q_m \partial q_{m'}} = \sum_i \frac{\partial^2 \ell_i}{\partial \lambda_i^2} \sum_j H_{ij} \frac{\partial f_j}{\partial q_m} \sum_{j'} H_{ij'} \frac{\partial f_{j'}}{\partial q_{m'}} + \sum_i \frac{\partial \ell_i}{\partial \lambda_i} \sum_j H_{ij} \frac{\partial^2 f_j}{\partial q_m \partial q_{m'}} \quad (\text{A30})$$

We treat the error of the resulting flux as having a log-normal distribution with a standard deviation given by the following expression:

$$\begin{aligned} \sigma_{\ln f^{(k)}(E)} &= \sqrt{\sum_m \sum_{m'} \frac{\partial \ln f^{(k)}}{\partial q_m^{(k)}} \text{cov}(q_m^{(k)}, q_{m'}^{(k)}) \frac{\partial \ln f^{(k)}}{\partial q_{m'}^{(k)}}} \\ &= \sqrt{\sum_m \sum_{m'} \frac{1}{f^{(k)}} \frac{\partial f^{(k)}}{\partial q_m^{(k)}} \text{cov}(q_m^{(k)}, q_{m'}^{(k)}) \frac{1}{f^{(k)}} \frac{\partial f^{(k)}}{\partial q_{m'}^{(k)}}} \end{aligned} \quad (\text{A31})$$

$$\text{cov}(q_m^{(k)}, q_{m'}^{(k)}) = \begin{pmatrix} \vdots & & \\ \dots & \frac{\partial^2 \ell^{(k)}}{\partial q_m \partial q_{m'}} & \dots \\ \vdots & & \end{pmatrix}^{-1} \quad (\text{A32})$$

To combine the multiple spectra into a single best fit spectrum we calculate a weighting,  $w$ , for each spectrum based on the penalty function,  $\ell^{(k)}$ , and number of free parameters,  $N_q$ :



$$w_k = \frac{\exp(-\ell^{(k)} - N_q^{(k)})}{\sum_k \exp(-\ell^{(k)} - N_q^{(k)})} \quad (\text{A33})$$

Finally, the weighted spectra are summed together to yield the following best-fit combined spectrum,  $\hat{f}(E)$ , with normalized error,  $\delta \ln \hat{f}(E)$  :

$$\ln \hat{f}(E) = \langle \ln f^{(\text{combined})}(E) \rangle = \sum_k w_k \ln f^{(k)}(E) \quad (\text{A34})$$

$$\begin{aligned} \delta \ln \hat{f}(E) &= \sqrt{\text{var} \ln f^{(\text{combined})}(E)} \\ &= \sqrt{\sum_k w_k \left( \sigma_{\ln f^{(k)}(E)}^2 + \ln^2 f^{(k)}(E) \right) - \langle \ln f^{(\text{combined})}(E) \rangle^2} \end{aligned} \quad (\text{A35})$$

To convert this into normal space flux and error on that flux the following is applied:

$$\hat{f}(E) = \exp \left( \ln \hat{f}(E) \right) \quad (\text{A36})$$

$$\hat{\sigma}(E) = \hat{f}(E) \cdot \delta \ln \hat{f}(E) \quad (\text{A37})$$

A representative example of the differences between the various single-function fits and the multi-function combined fit used for the MPE data set is presented in Figure 3. This figure shows results for a single NOAA15 observation on 13 May 2003 at L-shell 6.19. The left-hand panels show the various spectra used to make the combined fit as well as the combined fit spectrum itself. The right-hand panels display the corresponding count rates for each spectral fit, as well as the measured count rates (corrected for proton contamination; orange dots). The count rates corresponding to the various spectra are derived from the differential flux using a model that inverts each spectrum back to count rates in the four channels. The goal of the combined fit spectrum is to minimize the difference between the measured and derived count rates over all four channels. While this figure only displays a single measurement, it demonstrates large differences between the individual spectra and shows that count rates derived from the combined fit spectrum are closest to the measured count rates.

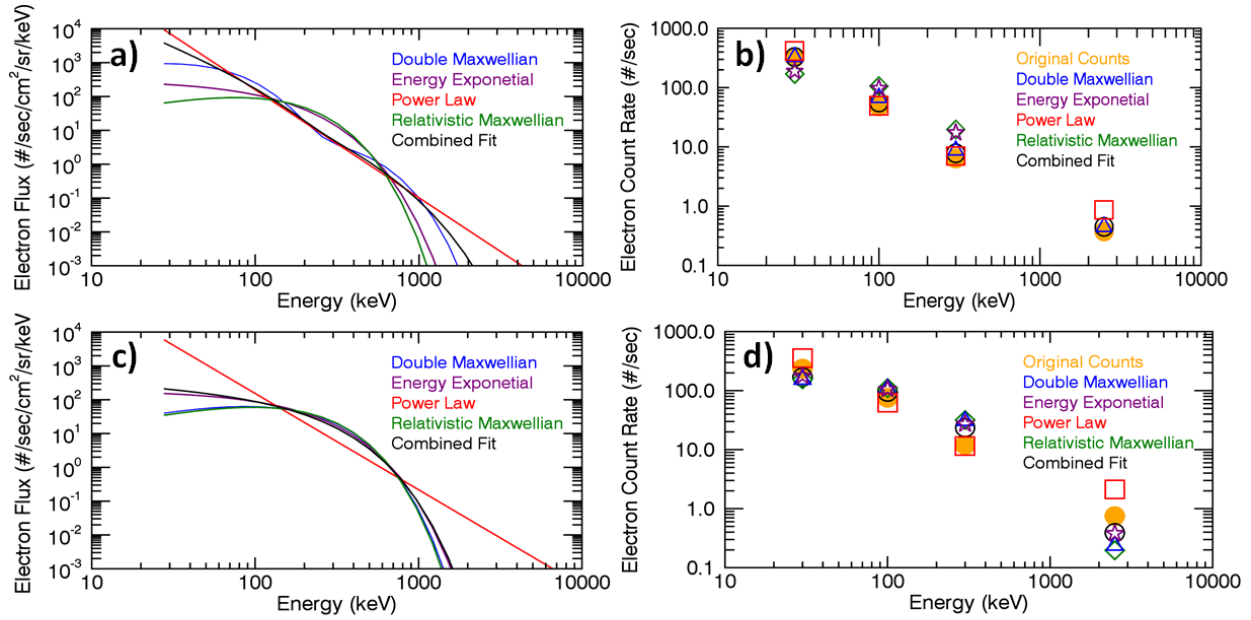


**Figure 3:** Comparison of differential electron flux spectra (a, c) calculated from NOAA15 MEPED measurements of electron count rates during one observation on 13 May 2003 at L-shell 6.19. Panels b and d show the observed (corrected) count rates (orange dots) as well as the count rates backed out from an inverse analysis of the spectra in panels a and c. The top panels (a, b) show results for the 0° telescope and the bottom panels (c, d) show results for the 90° telescope. The “combined fit” spectrum is used for the MPE data set.

To evaluate the different spectral fits more generally, the same method is performed using all MEPED measurements taken during 2003 between L-shells 4 and 8. Figure 4 displays these results for both the 0° telescope (top) and the 90° telescope (bottom). Median count rates within each electron channel, which have been derived from the different spectral fits as mentioned above, are presented in the left panels. Percent differences between the measured count rates and the count rates derived from the various spectra are shown in the right panels. Overall, count rates derived from the combined fit spectrum match the observed count rates better than the count rates derived from any of the individual spectral fits. These results demonstrate that the combined fit yields the smallest median differences from the measured count rates as well as the smallest interquartile range. The combined fit particularly outperforms the single function spectral fits in the E4 channel. The double Maxwellian shows the second smallest percent differences overall and outperforms the combined spectrum in the E1 channel for both detectors. However, it is worse in the E2, E3 and E4 channels. The power law spectrum shows fairly small percent differences for the 0° detector, but differences and interquartile ranges are larger in the 90° detector, particularly for the E1 and E4 channels. The energy exponential and relativistic Maxwellian show the largest percent differences in the 0° detector, with especially large differences and interquartile ranges in the E4 channel. While this is also true in the 90° detector, both show much better results overall, outperforming the power law spectrum, due to improved performance in the E1 channel. To summarize, while individual channels may show a specific fit to be better than the combined fit, Figure 4 shows

qualitatively that the combined fit most closely matches the observations when all four channels are considered together.

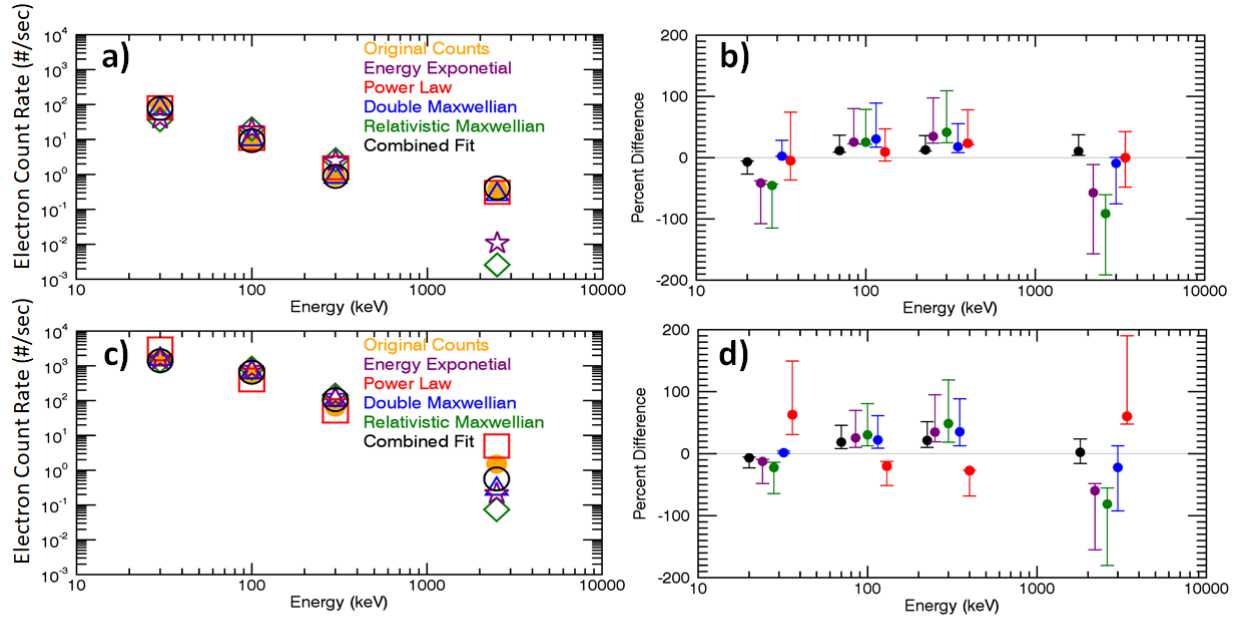


**Figure 4:** Statistical comparison of observed electron count rates in the E1-E4 channels ("Original Counts"), corrected for proton contamination, to count rates backed out from various spectral fits. Left panels (a, c) show median count rates in each electron channel for the 0° degree detector (a) and 90° degree detector (c) for all three satellites carrying MEPED instruments throughout 2003. Orange dots labeled "Original Counts" correspond to the corrected observations; open colored symbols correspond to the spectral fits noted in the legend. Right panels (b, d) show the percent differences between the backed out count rates and measured count rates as colored dots, colored according to the legend in panels a and c. Symbols in panels b and d are offset in energy for clarity. The interquartile ranges for each spectrum type are represented by the whiskers.

Results for all four electron channels are combined quantitatively by calculating the root mean square (RMS) fractional differences between the derived and observed count rates in the E1-E4 channels. Figure 5 shows the number distributions of the RMS differences for each of the four individual fits as well as for the combined fit, for the measurements included in Figure 4. Fractional differences, (calculated-observed)/observed, were used because the absolute differences in the E1 channel are much larger than the absolute differences in the E4 channel. Histograms of the RMS fractional differences are displayed in Figure 5 for both the 0° (panel a) and 90° (panel b) telescopes using all three available satellites carrying MEPED instruments during 2003. For both telescopes, the combined fit shows the highest number of small RMS fractional differences compared to any of the other individual fits, consistent with the results shown in Figure 4. Likewise, the double Maxwellian shows the second best fit overall. In the 0° telescope, the power law shows the third lowest RMS fractional differences. Both the energy exponential and relativistic Maxwellian show the most high fractional differences in the 0° detector. In the 90° telescope, the energy exponential and relativistic Maxwellian outperform the double Maxwellian fit in terms of higher number of the smallest RMS differences, but both fits have a skewed right-hand tail that allows for the double Maxwellian to remain the second best overall fit. The power law, which is often used as an assumed spectrum for MEPED data, shows the highest errors in 2003 with the 90° detector.

These results give confidence in the combined fit spectrum as the optimum fit to the MEPED data, in agreement with Peck et al. (2015). We do note, however, that this analysis cannot verify the goodness of fit outside the spectral range of the measurements.

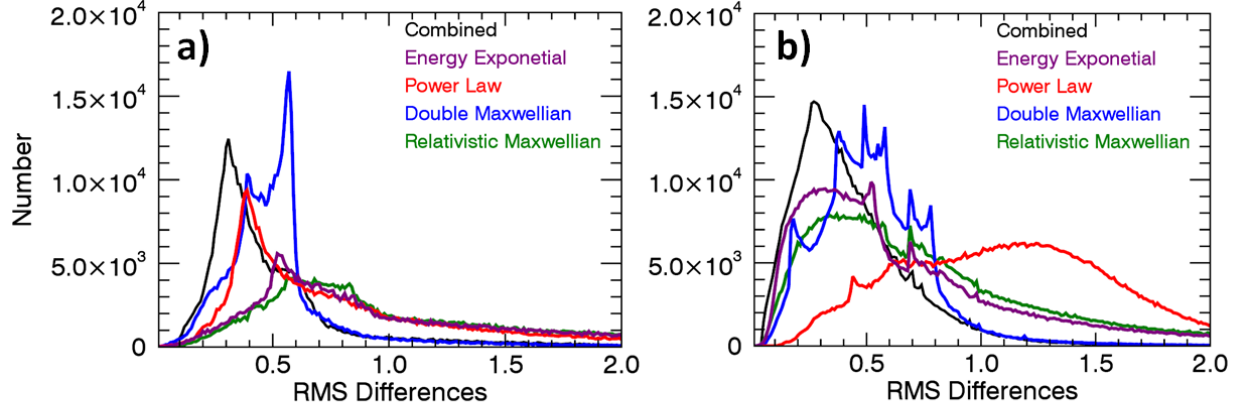


**Figure 5:** Number distributions of the root mean square (RMS) fractional differences between the count rates backed out from the various spectral fits and the corrected MEPED count rates, for the distribution of measurements in Figure 4. Panel (a) shows results for the  $0^\circ$  degree telescope and panel (b) shows results for the  $90^\circ$  telescope.

## B. Level 2 Data Product: Bounce-Loss Cone Flux

Once the differential electron flux is calculated and validated, the BLC flux can be estimated using the pitch angle of the instrument as well as the BLC edge angle calculated from the IGRF model. The result will be the estimated BLC flux calculated at each MEPED instrument measurement among all the satellites that are operational. One important differentiating aspect is whether the data sets incorporate one or both of the MEPED electron telescopes. The  $0^\circ$  detector views only part of the bounce loss cone (BLC), whereas the  $90^\circ$  detector views trapped, drift loss cone and BLC electron fluxes (*Rodger et al., 2010*). Electrons in the BLC are considered to be precipitating. Drift loss cone fluxes are considered to be trapped until they reach the South Atlantic Magnetic Anomaly (SAMA), where they will precipitate (*Gamble et al., 2008*). Trapped electrons may precipitate in the future, but are currently in stable mirroring pathways and are traveling pole-to-pole along magnetic field lines. Since it can be difficult to distinguish BLC fluxes from trapped or drift loss cone fluxes in the  $90^\circ$  detector, many available data sets include only the  $0^\circ$  detector, and thus have less information on the flux variation with pitch angle than when both detectors are used. At high latitudes the  $0^\circ$  detector is measuring exclusively BLC flux, at mid-latitudes a mixture of trapped and BLC flux and at low latitudes exclusively trapped flux. The opposite is true for the  $90^\circ$  detector (*Asikainen et al., 2019b*). Thus caution must be used to ensure that only the BLC flux in the detector measurements is being included, otherwise overestimation is likely. When calculating

both the drift-loss cone edge and the BLC edge using data from the International Geomagnetic Reference Field (IGRF) model (IAGA, 2010), we found that the BLC edge angle is smaller at all magnetic longitudes except within the SAMA. In an attempt to avoid drift-loss cone flux in our BLC calculations, we integrate only up to the BLC edge, and omit measurements in the SAMA. However, this may not eliminate possible drift-loss cone flux that may be present in the 90° degree data as shown in *Rodger et al.* (2010). Previous studies have shown that the 90° detector includes drift-loss cone flux at a variety of magnetic longitudes and pitch angles. Therefore, despite our attempt to remove the contaminating drift-loss cone flux in our BLC calculations, the use of the 90° detector may result in overestimation of electron fluxes at mid and lower latitudes where the 90° detector is measuring precipitating electrons.

The MPE data set includes both detectors by assuming a sinusoidal BLC angular distribution with maximum flux at a 90° pitch angle and zero flux at a 0° pitch angle. The sinusoidal function has been used in previous studies (*e.g.*, *Gu et al.*, 2011; *Vampola*, 1998) and is defined by Equation (1):

$$J_d(\alpha_{sat}) = A \sin^n(\alpha_{sat})$$

Here  $\alpha_{sat}$  is the pitch angle at the satellite location,  $A$  is the amplitude of the sine function and  $J_d$  is the measured electron flux. Because of the lack of available pitch angle data, we assume  $n$  is equal to 1. Upon solving for  $A$ , the total BLC flux is derived by integrating under the sine curve over the range of BLC pitch angles from 0° to  $\alpha_{BLC}$ . Here  $\alpha_{BLC}$  is the maximum BLC pitch angle and is calculated as:

$$\sin(\alpha_{BLC}) = \sqrt{B_{sat}/B_0}$$

where  $B_{sat}$  is the magnetic field strength at the satellite altitude and  $B_0$  is the magnetic field strength at 120 km. The magnetic field strength is calculated from the IGRF model (IAGA, 2010). On occasion, however, the relative count rates in the two detectors violate the assumption that count rates vs. pitch angle should vary as a sine function in the BLC. This occurs when the detector with the lower pitch angle has a higher flux. For these measurements the MPE data set includes only the detector that has the lower pitch angle.

---

### C. Level 3 Data Product: Global BLC Flux Maps

The final product takes the BLC flux calculated in the Level 2 product as uses Delaunay triangulation to interpolate global BLC flux maps as a function of energy. Since the MPE data product is calculated on 27 energy bins, the Level 3 data product will contain 27 global maps. The precipitating electron flux spectra at the MEPED sampling locations are combined into daily, global maps. For each day 27 maps are constructed, one for each energy bin (see Figure 2), using a 2° magnetic latitude × 2° magnetic longitude

grid. The MPE mapping uses Delaunay triangulation (*Delaunay et al., 1934*) to interpolate in space between the measurements on the day in question. In contrast, the mapping method employed for the MP15 data set used a linear interpolation that required between 3 and 7 days of data to populate each  $2^\circ \times 2^\circ$  bin. The MP15 maps are thus compromised by electron fluxes that are elevated before or after events due to the multi-day averaging. Other MEPED-based precipitating electron data sets, such as the CMIP6 data set, assume zonal averages on L-shells, and thus do not capture variations in magnetic longitude. Delaunay triangulation was chosen for the MPE data set because it captures small scale features that are obscured by other mapping methods.

Figure 6 compares the derived 28-keV (top) and 779-keV (bottom) precipitating electron flux at the satellite locations (a, d) to the gridded flux from the MP15 (b, e) and MPE (c, f) mapping methods for 1 May 2003; all maps are shown in geomagnetic coordinates. To ensure the MP15 and MPE maps include the same data, only one day of MEPED data is included in the MP15 map. MEPED observations do not include the geographic pole, which results in the data void regions in panels (a) and (d) that are offset from the geomagnetic pole. Since the interpolation used in the MP15 mapping does not allow for interpolation across the geomagnetic pole, the MP15 maps include a data void region from  $83^\circ$  magnetic latitude to the magnetic pole. The MPE mapping method interpolates across the geomagnetic pole by assuming zonal averages in order to fill in this small region (e.g., in Figure 6c and 6f, near geomagnetic latitude  $83^\circ$ S and  $0^\circ$  magnetic longitude). The comparisons in Figure 6 indicate that because of the Delaunay triangulation, the MPE maps capture more of the observed small-scale variations than maps based on the MP15 interpolation or L-shell binning methods. However, some of the small-scale structures in the MPE maps are caused by artifacts of interpolation over regions with incomplete satellite measurement coverage; there were often gaps in magnetic local time coverage in 2003, when only three MEPED satellites were operating. For most of the MEPED data record at least 5 satellites are available, so data gaps are smaller. The advantage of using Delaunay triangulation to map the data is that it can capture small-scale features such as sub-storm activity that would be averaged out in other data sets. There is a disadvantage in that sub-storm activity will effectively persist for a day at a time since the maps have one-day resolution; in reality, these storms most likely have durations of minutes to hours (*Cresswell-Moorcock et al., 2013; Beharrell et al., 2015; Partamies et al., 2021*). On the other hand, it is likely that not all substorms are observed, particularly in a year like 2003 when only three POES satellites were operational. While the triangulation mapping method used in MPE would not be able to capture all substorm activity, its ability to capture some substorm activity is a significant improvement over zonal averaging, which is typically done using MEPED data.

Finally, it is noteworthy that the MPE data set has been adapted for use during SPEs. During SPEs, the MEPED data become unreliable due to significant proton contamination. Therefore, most EEP data sets remove days when SPEs occur. The MPE data set instead uses monthly averaged electron flux maps for days when SPEs occur. This is done by taking the maps from the 15 days before and the 15 days after the day the SPE occurs and averaging them together to produce a map for the day of the SPE. When multiple SPE days occur within the monthly time frame, those days are removed before the average is calculated. This is important since SPEs occur during times of high geomagnetic activity, so removing the SPE days from the data set would cause the electron precipitation to be less accurate during these days. By setting the precipitating electron flux to monthly average values instead of removing them, the MPE data set reduces this inaccuracy.

---

## D. Data Arrays

Below gives a detailed description of all the variable arrays available for an arbitrary day for the Level-1 data.

```
dimensions:
  energy = 27;
  proton_telescopes = 6;
  electron_telescopes = 3;
  electron_telescopes_and_E4 = 4;
  2_Parameter_Spectrum = 2;
  4_Parameter_Spectrum = 4;
  number_of_spectra = 4;
  time = UNLIMITED; // (5400 currently)

variables:
  int flag(time=5400);
    :Full_Name = "Flag Strange Spectral Fits";

  double time(time=5400);
    :Full_Name = "Time of measurment";
    :Units = "milliseconds since 1970 (I know...)";

  double rtime(time=5400);
    :Full_Name = "Time of measurement";
    :Units = "hours";

  double geogLat(time=5400);
    :Full_Name = "Satellite Geographic Latitude";
    :Units = "degrees -90 to 90";

  double geogLon(time=5400);
    :Full_Name = "Satellite Geographic Longitude";
```



```

:Units = "degrees 0 to 360";

double foflLat(time=5400);
:Full_Name = "Satellite Foot of the Field Line Geographic Latitude";
:Units = "degrees -90 to 90";

double foflLon(time=5400);
:Full_Name = "Satellite Foot of the Field Line Geographic Longitude";
:Units = "degrees 0 to 360";

double MLT(time=5400);
:Full_Name = "Satellite Magnetic Longitude";
:Units = "degrees 0 to 360";

double lValue(time=5400);
:Full_Name = "Satellite L-Value";
:Units = " ";

float energy(energy=27);
:Full_Name = "Center Energy of Electron/Proton Fluxes";
:Units = "KeV";

double EOcounts(time=5400, electron_telescopes=3);
:Full_Name = "Original Electron Count Rate";
:Units = "counts/sec";

double Proton_Contamination(time=5400, electron_telescopes=3);
:Bad_Data_Value = -999.0; // double

double EOcounts_Lambda(time=5400, electron_telescopes_and_E4=4);
:Full_Name = "Forward Model Corrected Electron Count Rate";
:Units = "counts/sec";

double EOcounts_corrected(time=5400, electron_telescopes_and_E4=4);
:Full_Name = "Corrected Electron Count Rate";
:Units = "counts/sec";

double POcounts(time=5400, proton_telescopes=6);
:Full_Name = "Original Proton Count Rate";
:Units = "counts/sec";

double POcounts_Lambda(time=5400, proton_telescopes=6);
:Full_Name = "Forward Model Proton Count Rate";
:Units = "counts/sec";

double Ecounts(time=5400, energy=27);
:Full_Name = "Corrected Electron Flux Rate";
:Units = "N/cm^2/sr/keV";
:Bad_Data_Value = -999.0; // double

double Pcounts(time=5400, energy=27);
:Full_Name = "Corrected Proton Flux Rate";
:Units = "N/cm^2/sr/keV";
:Bad_Data_Value = -999.0; // double

double Eerror(time=5400, energy=27);
:Full_Name = "Error on Corrected Electron Count Rate, 1-sigma";

```

```

:Units = "N/cm^2/sr/keV";

double Perror(time=5400, energy=27);
:Full_Name = "Error on Corrected Proton Count Rate, 1-sigma";
:Units = "N/cm^2/sr/keV";

double ERMq(time=5400, 2_Parameter_Spectrum=2);
:Full_Name = "Parameters for Electron Relativistic Maxwellian
Spectrum";
:Spectrum_Equation = "f(E) = E*(1 + E/E0/2)*exp(q1 + q2*E)";
:Rest_Energy = "E0 = 511 keV";

double EPLq(time=5400, 2_Parameter_Spectrum=2);
:Full_Name = "Parameters for Electron Power Law Spectrum";
:Spectrum_Equation = "f(E) = exp(q1 - q2*ln(E))";

double EEQq(time=5400, 2_Parameter_Spectrum=2);
:Full_Name = "Parameters for Electron Energy Exponential Spectrum";
:Spectrum_Equation = "f(E) = exp(q1 + q2*E)";

double EDMq(time=5400, 4_Parameter_Spectrum=4);
:Full_Name = "Parameters for Electron Double Relativistic Maxwellian
Spectrum";
:Spectrum_Equation = "f(E) = E*(1 + E/E0/2)*[exp(q1 + q2*E)+exp(q3 +
q4*E)]";
:Rest_Energy = "E0 = 511 keV";

double PRMq(time=5400, 2_Parameter_Spectrum=2);
:Full_Name = "Parameters for Proton Relativistic Maxwellian Spectrum";
:Spectrum_Equation = "f(E) = E*(1 + E/E0/2)*exp(q1 + q2*E)";
:Rest_Energy = "E0 = 938 MeV";

double PPLq(time=5400, 2_Parameter_Spectrum=2);
:Full_Name = "Parameters for Proton Power Law Spectrum";
:Spectrum_Equation = "f(E) = exp(q1 - q2*ln(E))";

double PEEq(time=5400, 2_Parameter_Spectrum=2);
:Full_Name = "Parameters for Proton Energy Exponential Spectrum";
:Spectrum_Equation = "f(E) = exp(q1 + q2*E)";

double PDMq(time=5400, 4_Parameter_Spectrum=4);
:Full_Name = "Parameters for Proton Double Relativistic Maxwellian
Spectrum";
:Spectrum_Equation = "f(E) = E*(1 + E/E0/2)*[exp(q1 + q2*E)+exp(q3 +
q4*E)]";
:Rest_Energy = "E0 = 938 MeV";

double W(time=5400, number_of_spectra=4);
:Full_Name = "Weighting of Log Electron Fluxes";
:Order_of_elements = "Relativistic Maxwellian, Power Law, Exponential,
and Double Relativistic Maxwellian";
:How_to_use = "Multiply respective elements to ln of spectra, sum
products together, and exp to get combined spectrum.";

double Wp(time=5400, number_of_spectra=4);
:Full_Name = "Weighting of Log Proton Fluxes";

```

```

:Order_of_elements = "Relativistic Maxwellian, Power Law, Exponential,
and Double Relativistic Maxwellian";
:How_to_use = "Multiply respective elements to ln of spectra, sum
products together, and exp to get combined spectrum.";

double pitch(time=5400);
:Full_Name = "Pitch Angle";
:Units = "degrees -180 to 180";

double Bfofl(time=5400);
:Full_Name = "Magnetic Field Strength at 120km";
:Units = "Tesla";

double Blocal(time=5400);
:Full_Name = "Magnetic Field Strength at Satellite";
:Units = " ";

double BLC_Angle(time=5400);
:Full_Name = "Bounce-Loss Cone Angle";
:Units = "degrees";

```

---

## E. References

Asikainen, T., & Ruopsa, M. (2019). New Homogeneous Composite of Energetic Electron Fluxes From POES: 2. Intercalibration of SEM-1 and SEM-2. *Journal of Geophysical Research: Space Physics*, 124, 1203–1221. <https://doi.org/10.1029/2018JA026214>

Asikainen, T. (2019). New homogeneous composite of energetic electron fluxes from POES: 2. Intercalibration of SEM-1 and SEM-2. *Journal of Geophysical Research: Space Physics*, 124, 5761–5782. <https://doi.org/10.1029/2019JA026699>

Beharrell, M. J., F. Honary, C. J. Rodger, and M. A. Clilverd (2015), Substorm-induced energetic electron precipitation: Morphology and prediction, *J. Geophys. Res. Space Physics*, 120, 2993–3008, doi:10.1002/2014JA020632

Cresswell-Moorcock, K., C. J. Rodger, A. Kero, A. B. Collier, M. A. Clilverd, I. Häggström, and T. Pitkänen (2013), A reexamination of latitudinal limits of substorm-produced energetic electron precipitation, *J. Geophys. Res. Space Physics*, 118, 6694–6705, doi:10.1002/jgra.50598

Delaunay, B., (1934). Sur la sphère vide. A la mémoire de Georges Voronoï. *Bulletin de l'Académie des Sciences de l'URSS. Classe des sciences mathématiques*, Issue 6, 793–800

Evans, D. S., & Greer, M. S. (2006). Polar orbiting environmental satellite space environment monitor-2: Instrument descriptions and archive data documentation. *NOAA Technical Memorandum 1.4*, Space Environment Center, Boulder, Colo.

Gu, X., Zhao, Z., Ni, B., Shprits, Y., & Zhou, C., (2011). Statistical analysis of pitch angle distribution of radiation belt energetic electrons near the geostationary orbit: CRRES observations. *Journal of Geophysical Research*, 116, A01208. <https://doi.org/10.1029/2010JA016052>

Partamies, N., Tesema, F., Bland, E., Heino, E., Nesse Tyssøy, H., and Kallelid, E.: Electron precipitation characteristics during isolated, compound, and multi-night substorm events, *Ann. Geophys.*, 39, 69–83, <https://doi.org/10.5194/angeo-39-69-2021>, 2021.

Rodger, C. J., Clilverd, M. A., Green, J. C., & Lam M. M., (2010a). Use of POES SEM-2 observations to examine radiation belt dynamics and energetic electron precipitation into the atmosphere. *Journal of Geophysical Research: Space Physics*, 115, A04202. <https://doi.org/10.1029/2008JA014023>

Vampola, A. L. (1998). Outer zone energetic electron environment update, in Conference on the High Energy Radiation Background in Space, 128–136, IEEE Press, Piscataway, N.J. <https://doi.org/10.1109/CHERBS.1997.660263>

Yando, K., Millan, R. M., Green, J. C., & D. S. Evans (2011). A Monte Carlo simulation of the NOAA POES Medium Energy Proton and Electron Detector instrument. *Journal of Geophysical Research*, 116, A10231. <https://doi.org/10.1029/2011JA016671>